LASER & PHOTONICS REVIEWS

www.lpr-journal.org

Quasi-Bound States in the Continuum Enhanced Second-Harmonic Generation in Thin-Film Lithium Niobate

Xiaotian Zhang, Linye He, Xin Gan, Xiaocong Huang, Yixuan Du, Zhenshan Zhai, Zhuang Li, Yuanlin Zheng, Xianfeng Chen, Yangjian Cai, and Xianyu Ao**

This work reports the second-harmonic generation (SHG) in a *z*-cut thin-film lithium niobate (LN) under nearly normal-incident linearly-polarized pumping. To utilize the largest nonlinear term which is along the out-of-plane direction in the *z*-cut LN film, the film is patterned with a 2D periodic array to support symmetry-protected bound states in the continuum (BICs) bearing strong out-of-plane electric field component. Enabled by such optical resonances near the BIC condition at the pumping wavelength, significant enhancement in SHG compared to an unpatterned film is observed. This approach, combining transparent thin-film nonlinear materials with tailored BICs, offers prospects for engineering compact coherent light sources in a broad wavelength range.

1. Introduction

Lithium niobate (LN) features excellent piezoelectric, electro-optic, photorefractive, and nonlinear optical effects. Most importantly, LN is optically transparent in a wide spectral range spanning from ultraviolet to the mid-infrared with a moderate refractive index (≈ 2.2 in the visible regime). These outstanding optical properties make LN a versatile material in optoelectronics and nonlinear optics. For instance, LN electro-optic modulators have played a key role in high-speed optical communication networks,[1–4] and periodically poled LN has been widely used for second-order nonlinear frequency conversion.[5] As the nonlinear optical effects are intrinsically weak, traditional bulk LN nonlinear devices require long interaction lengths together with phase matching to achieve efficient conversion. With breakthroughs in fabrication techniques, thin-film LN cleaved from bulk crystals through ion slicing and wafer bonding onto silica-coated substrates have been made commercially available. Such a thin-film LN on insulator (LNOI) platform,[6–10] contrary to bulk counterparts, can provide much higher optical mode confinement to render a shorter interaction length. As for nonlinear optical frequency conversion, second-harmonic generation (SHG) has been demonstrated in thin-film LN waveguides,[11–17] microring cavities,[18,19] microdisk cavities,[20–25] photonic crystal cavities,[26–28] and Bragg cavities.[29] Among them, cavities usually are resonant at least at the pump wavelength, leading to strong and efficient nonlinear optical interactions.

When considering free-space coupling with pump beams impinging upon the nonlinear device along the film thickness direction, the characteristic distance of interactions can be at the sub-wavelength scale. In this regime, the nonlinear conversion can be dramatically promoted via the recently emerged concepts of anapole[30–32] and bound states in the continuum (BICs)[33–40] in nanophotonics. The term anapole refers to a configuration of electromagnetic fields with zero net dipolar radiation.[41–43] On the other hand, BICs[44] are nonradiating eigenmode of an open system. Excitation of such nonradiating configurations or states can suppress radiative losses, create strong near-field enhancements inside nonlinear nanostructures at the pump wavelength and thus amplify the effective power exciting the nonlinear processes. Particularly, spatially extended BIC modes in 2D periodic arrays are of special interest for enhancing nonlinear optical processes, as they allow the thin-film volume of nonlinear materials to be well exploited.[33–39] Furthermore, strict phase-matching is not required in such thin resonant nanostructures. In practice, BICs degrade into quasi-BICs with a limited yet still high quality (Q) factor, due to structure imperfections and finite extent, or by breaking the in-plane inversion symmetry intentionally.[45] As for LN, resonantly enhanced SHG has been demonstrated using bright modes in periodic arrays composed of in-plane symmetric unit cells such as 1D gratings[46] and 2D cone arrays,[47,48] however, the field enhancement by such broad resonances was moderate. The experimental realization of BICs in LN is rare,[49] despite the fact that several numerical studies showed the potential

X. Zhang, Y. Du, Z. Zhai, Z. Li, Y. Cai, X. Ao
Shandong Provincial Engineering and Technical Center of Light Manipulation & Shandong Provincial Key Laboratory of Optics and Photonic Devices
School of Physics and Electronics
Shandong Normal University
Jinan 250358, China
E-mail: yangjiancai@sdnu.edu.cn; aox@sdnu.edu.cn

L. He, X. Gan, X. Huang
Centre for Optical and Electromagnetic Research
South China Academy of Advanced Optoelectronics
South China Normal University
Guangzhou 510006, China

Y. Zheng, X. Chen
State Key Laboratory of Advanced Optical Communication Systems and Networks
School of Physics and Astronomy
Shanghai Jiao Tong University
Shanghai 200240, China

The ORCID identification number(s) for the author(s) of this article can be found under https://doi.org/10.1002/lpor.202200031

DOI: 10.1002/lpor.202200031

of quasi-BICs[50–52] (and also anapole[53]) for thin-film LN-based nonlinear resonant nanophotonics.

In this work, we report symmetry-protected BICs in a *z*-cut LN thin film patterned with 2D periodic nanostructures, and demonstrate resonantly enhanced SHG under nearly normal-incident linearly-polarized pumping. The SHG enhancement is mainly driven by the optical resonances at the pump wavelength. The largest nonlinear coefficient in the *z*-cut LN thin film is along the out-of-plane direction, while the involved quasi-BIC modes possess strong out-of-plane electric field component and thus can efficiently couple the pumping electric fields to the out-of-plane component of the nonlinear polarization. Here the 2D periodic array on thin-film lithium niobate was defined by soft lithography over a large area. The high near-field enhancement within the nanostructures resulted in more than 400 times enhancement of SHG compared to the flat LN thin film. The connection between the quasi-BIC modes and the SHG enhancement was confirmed by the correlation between angle-resolved measurements of white-light transmission and second-harmonic (SH) emission.

2. Results and Discussion

Figure 1a depicts our thin-film LN device, consisting of a square lattice of LN cones on a residual LN film. The conic shape is a result of dry etching. We fabricated the nanostructure using 680 nm thick *z*-cut LN thin film bonded on 2 μm thick silica on silicon substrate (NanoLN). Figure 1b illustrates the fabrication procedure. Briefly, a square array of high-aspect-ratio photoresist nanopillars was first defined on the LN wafer by solvent-assisted nanoscale embossing, using a poly-(dimethylsiloxane) (PDMS) stamp containing the negative surface structure of the photoresist pillars (the stamp was created in a previous publication[54]). Since the *z*-cut LN film is isotropic in the device plane, no special care was required for mask alignment. The etching of LN was performed using inductively coupled plasma (ICP) with photoresist nanopillars as the etching mask. Figure 1c shows the photograph of the fabricated sample. Scanning electron microscopy (SEM) images of the fabricated LN structure are shown in Figure 1d. We estimated that the cones had a top radius $r_1 = 245$ nm, bottom radius $r_2 = 350$ nm, height $h = 350$ nm, and lattice spacing $a_0 = 720$ nm, although the actual structure deviated from ideal cylindrical cone shapes.

Such a periodic system supports symmetry-protected BICs with an infinite quality factor at Γ point of the irreducible Brillouin zone, as the singly degenerate modes shown in **Figure 2**a,b. Here the system (without considering the silicon substrate) was modelled using a 3D finite-element eigenfrequency solver (COMSOL multiphysics), by setting up a unit cell surrounded with absorbing boundary conditions on the top and bottom surfaces of the computational domain, and Bloch boundary conditions on the remaining surfaces. The singly degenerate modes *A*, *B*, *C*, and *D* at Γ point are decoupled from the external radiation continuum due to symmetry mismatch (Figure 2b), but can become observable when the mirror symmetry is broken, caused by, for example, off-normal incidence. Due to the slab geometry, one set (*A* and *B*) degrades into quasi-BICs excitable by TE-polarized light at off-normal incidence; while the other set (*C* and *D*) degrades into quasi-BICs excitable by TM-polarized light at off-normal incidence. We focus on the latter because the largest nonlinear coefficient d_{33} in the *z*-cut LN film is along the out-of-plane direction, and the quasi-BIC modes evolved from mode *C* and mode *D* have strong E_z-component which might be utilized to convert the incident linearly-polarized pump efficiently into the *z*-component of the nonlinear polarization as

$$P_z^{\mathrm{NL}} \propto d_{31}\left(E_x^2 + E_y^2\right) + d_{33}E_z^2 \tag{1}$$

Figure 2c shows the simulated angle-resolved zero-order transmission spectra under TM polarization, mapping out the same TM dispersion bands as the red lines along ΓX in Figure 2a. The BIC modes are manifested by spectral narrowing and

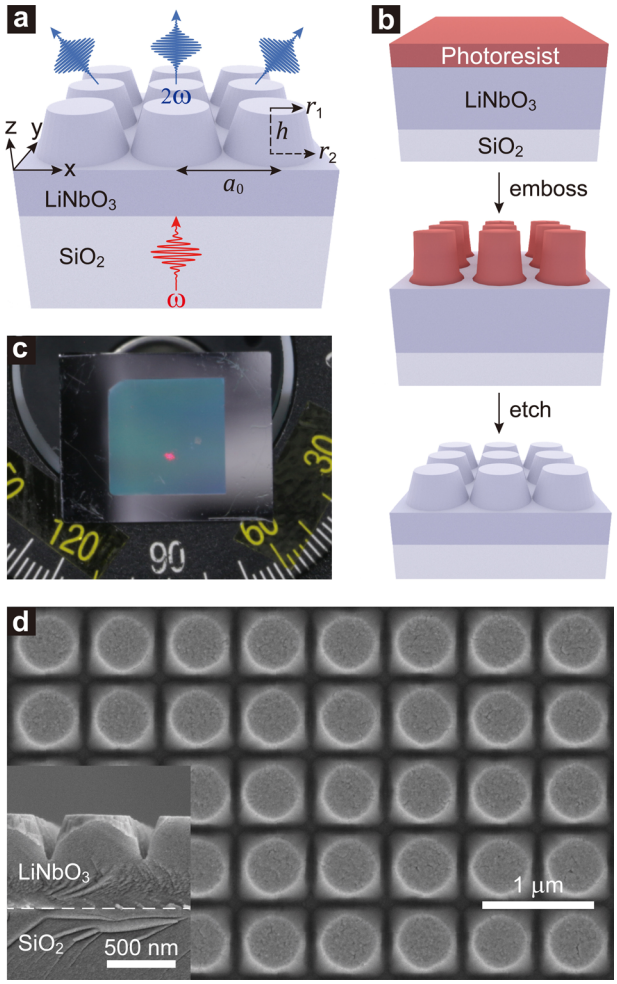

Figure 1. Design and fabrication of the thin-film $LiNbO_3$ nonlinear device. a) Schematic of the array structure consisting of a square lattice of $LiNbO_3$ cones on a residual $LiNbO_3$ film. The extraordinary axis of $LiNbO_3$ is along the *z*-axis. The pump beam impinges on the device from the substrate side, and the second-harmonic is collected in the forward direction. b) Main steps of the fabrication process. c) Photograph of the sample. The patterned area is 1 cm × 1 cm. The red spot on the patterned area is the second-harmonic emission pumped by femtosecond pulses around 1300 nm wavelength. d) Cross-sectional and top-view SEM images of the fabricated $LiNbO_3$ structure. The $LiNbO_3$ cones (with top radius $r_1 = 245$ nm, bottom radius $r_2 = 350$ nm, and height $h = 350$ nm) are arranged in a square lattice (with the center to center spacing $a_0 = 720$ nm) on a residual $LiNbO_3$ layer of 330 nm thick.

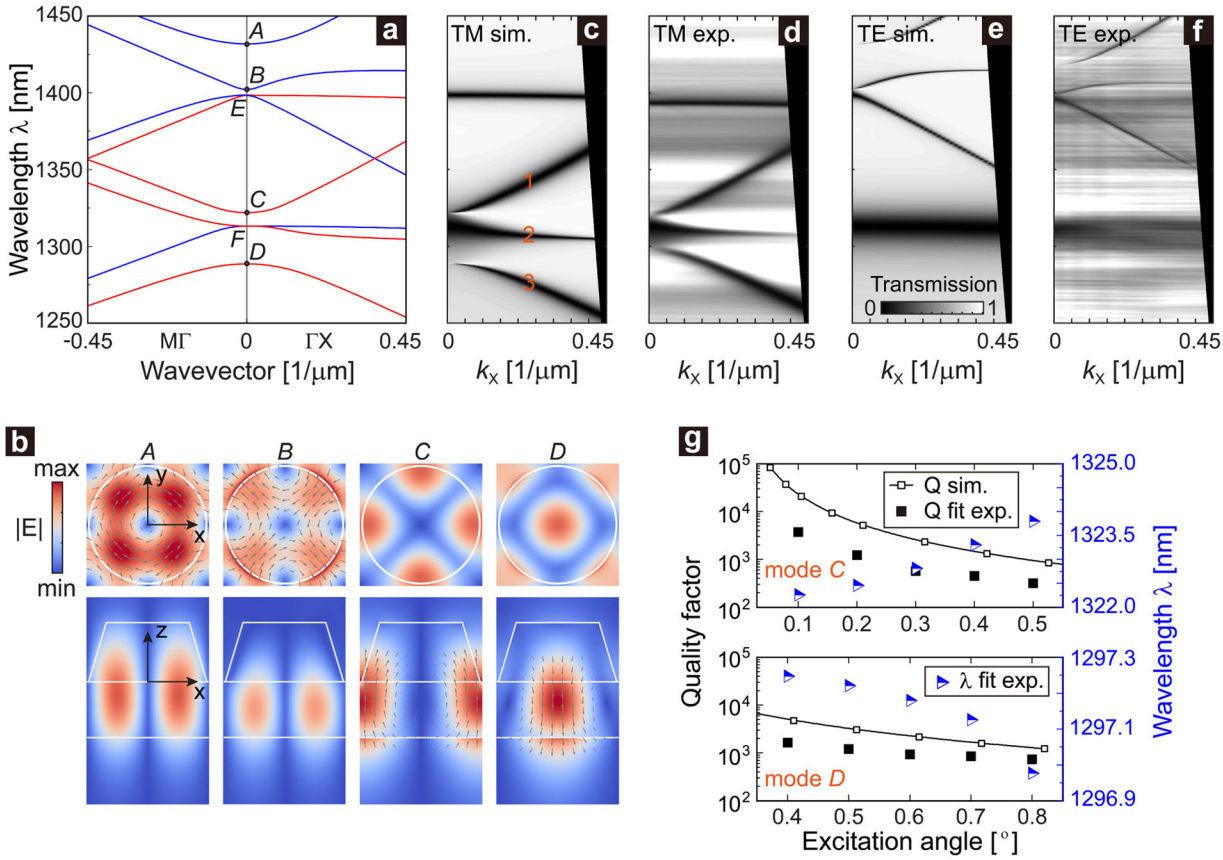

Figure 2. Quasi-BICs evolved from the singly degenerate modes. a) Band structure of the square lattice of $LiNbO_3$ cones (top radius r_1 = 245 nm, bottom radius r_2 = 350 nm, height h = 350 nm, lattice spacing a_0 = 720 nm, on a residual $LiNbO_3$ layer of 330 nm). b) Electric field distributions in one unit cell for the four singly degenerate modes at Γ point. The direction of the electric field is indicated with gray arrows. c,d) Simulated and measured angle-resolved transmission spectra under TM-polarized plane-wave excitation. e,f) Simulated and measured angle-resolved transmission spectra under TE-polarized plane-wave excitation. g) Angular dependence of the extracted quality factors and resonance wavelengths for mode *C* and mode *D*. The quality factors from simulation are also shown for reference.

vanishing transmission as k_x approaches zero (bands 1 and 3 in Figure 2c). In other words, the *Q* factor of the quasi-BIC modes decreases rapidly when k_x is away from Γ (Figure S1, Supporting Information). The measured TM transmission spectra from the fabricated sample under collimated white-light illumination are shown in Figure 2d, and the one-to-one correspondence with simulation in Figure 2c allows us to unambiguously identify the quasi-BIC modes in the experiment. In the measurement, mode *C* and mode *D* appeared around λ_C = 1322 nm and λ_D = 1298 nm, respectively. (For completeness, the simulated and measured transmission spectra under TE polarization are shown in Figure 2e,f. Note that the broad resonance in between mode *C* and mode *D* can contribute to SHG as shown below.) Figure 2g shows the *Q* factors extracted from fitting the measured transmission spectra, together with *Q* factors from finite-element simulation. Overall, the experimental *Q* factors were about one order of magnitude smaller than the theoretical ones, and both showed a similar decreasing trend when the excitation angles became larger. The experimental *Q* factors can be over 1000 when excitation angles < 0.2° for the mode around λ_C = 1322 nm (or when excitation angles < 0.5° for the mode around λ_D = 1298 nm). In reality, surface roughness and spatial disorder can degrade the *Q* factor of the quasi-BIC modes.[55] Because mode *B* and mode *C* had enhanced fields distributed close to the cone surface, their *Q* factors were more sensitive to the local change of the cone shape (Figure S1, Supporting Information). Therefore, the *Q* factor of mode *C* deviated much more from the corresponding theoretical expectation than mode *D* did.

When these high-*Q* modes near BIC conditions are excited by external waves resonantly, the optical fields inside the nanostructures can be dramatically amplified (Figure S2, Supporting Information). As the *z*-component of the electric field at the pump wavelength is expected to be most relevant for SHG in our device, we further show in Figure S3 (Supporting Information) the intensity enhancement of E_z averaged in the LN volume, calculated under excitation of TM-polarized plane waves. For band 1 and band 3, the volume-averaged intensity enhancement of E_z can be over 1000 when excitation angles approached zero, and dropped by one order of magnitude within 0.5° angles. When the pump wavelength is aligned with these resonance wavelengths, the resulting giant pump intensity inside the nonlinear nanostructure can boost the nonlinear optical processes with enhancement of several orders of magnitude (Figure S4, Supporting Information).

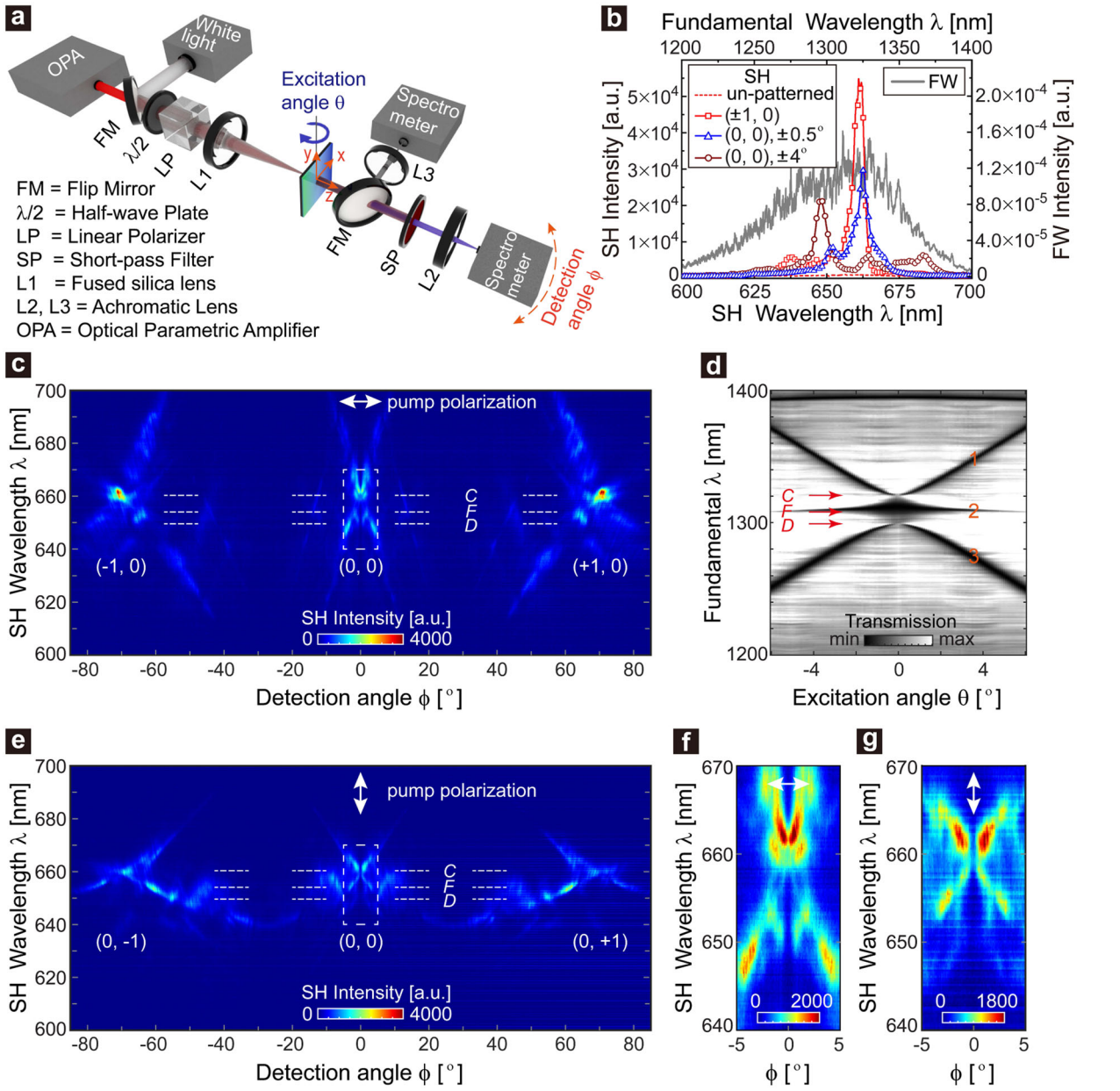

Figure 3. Nonlinear emission from the $LiNbO_3$ device. a) Setup for SH emission and white-light transmission measurement. The sample is mounted on a rotational stage to change the excitation angle θ (within the horizontal *xz*-plane). The optical elements after the sample are mounted on another rotational stage to change the detection angle ϕ (within the horizontal *xz*-plane). b) SH emission spectra from patterned and un-patterned areas. The spectra of the OPA beam at the sample position are also shown for reference. c) Angle-resolved SH emission spectra showing the diffraction orders for horizontal pump polarization. The white dashed lines mark the half-wavelength positions of mode *C*, *F*, and *D*. d) White-light transmission spectra for horizontal (TM) input polarization when changing the excitation angle. e) Angle-resolved SH emission spectra showing the diffraction orders for vertical pump polarization. f,g) Enlarged views of the central regions in (c) and (e).

To characterize the SH emission properties, we employed broadband pulses from an optical parametric amplifier (OPA) to excite SHG (based on the rotational stages shown in **Figure 3**a). The spectra of the excitation beam at the sample position are shown in Figure 3b, which covered both mode *C* and mode *D*. The excitation was incident from the silicon substrate side, and the SH emission was collected in the forward direction. The sample was put at a distance away from the focus to prevent burns, and thus the excitation beam was divergent and carried components with nonzero transverse wavevectors. When the input pump polarization is horizontal, the dispersion exhibits the characteristic of TM polarization within the horizontal *xz*-plane (and TE polarization within the vertical *yz*-plane). For the SH emission shown below, the sample was kept at the excitation angle of 0°, and the detector was scanned within the horizontal *xz*-plane to measure the angle-resolved emission spectra.

Figure 3c shows the angle-resolved emission spectra with horizontal pump polarization. The SH emission is governed by the nonlinear polarization together with the diffraction property of the periodic array at SH wavelengths.[47,48] As our periodic LN nanostructure had a lattice spacing larger than the SH wavelength, the SH emission exhibited four first-order diffraction beams, in addition to the central beam close to the surface normal. The strongest SH emission was the (±1, 0) diffraction orders with peak wavelength λ_{SH} = 662 nm. To unveil how SHG depends on the quasi-BIC modes at the fundamental wavelengths, we show the white-light transmission side by side (Figure 3d). The SH emission peak at λ_{SH} = 662 nm can be unambiguously attributed to the off-normal quasi-BIC modes evolved from mode *C*, with the corresponding fundamental wavelength (FW) $\lambda_{FW} = 2\lambda_{SH}$ slightly longer than λ_C = 1322 nm. For $\lambda_{SH} \approx \lambda_D/2$, only the (0,0) diffraction order was clearly visible, which appeared at $\phi = \pm 4°$. We noticed that there were also SH spots with $\lambda_{FW} \approx$ 1310 nm, corresponding to the broad resonance (denoted as mode *F*) lied in between mode *C* and mode *D*, and both (0, 0) and (±1, 0) diffraction orders were visible. This mode *F* is doubly degenerate (Figure 2a), and therefore can be excited by either TM- or TE-polarized light with slightly different dispersion at off-normal angles.

To assess the (0, ±1) diffraction orders equivalently, we switched the pump polarization to be vertical, and summarized the angle-resolved emission spectra in Figure 3e. Around the wavelength of 660 nm the (0, ±1) and (0, 0) diffraction orders exhibited an intensity of similar level. It might be counter-intuitive to see that the (0, ±1)-order spots corresponding to mode *F* showed an intensity stronger than the other spots caused by quasi-BIC modes, since the field enhancement of mode *F* was moderate (Figure S2, Supporting Information). It should be pointed out that the linewidth of mode *F* was broad and thus matched better with the spectral bandwidth of the pump, resulting in a relatively high total intensity.

In order to estimate the enhancement induced by the nanostructure, we increased the integration time of the spectrometer to make the SH emission spectra from the unpatterned area visible (shown as the dashed line in Figure 3b), and also captured the spectra at the angular positions exhibiting peak intensity in Figure 3c with the same integration time (shown as the lines with markers in Figure 3b). For $\lambda_{SH} \approx$ 662 nm, we found that the ratio between the peak intensity of the (±1, 0)-order spots and that from the un-patterned area was $I_{(\pm1,\,0)}/I_{\text{un-patterned}} \approx 125$, while $I_{(0,\,0)} \approx I_{(0,\,\pm1)} \approx 0.5 I_{(\pm1,\,0)}$. Therefore, we observed a total SHG enhancement of over 400 times for the patterned area relative to the un-patterned area. It should be pointed out that, this enhancement was estimated based on the spectra at certain angles relative to the spectra along the surface normal from the un-patterned area, not the energy integrated over the solid angle of a hemisphere. A further comparison of the enhancements between mode *C* and mode *D* was hindered by the fact that the spectral bandwidth of our pump was much broader than the linewidth of the quasi-BIC modes. We had not intended to optimize the structure experimentally. Simulations showed that both the *Q* factor and the peak SHG efficiency can vary considerably when the thickness of the residual LN layer changes (Figure S5, Supporting Information). Moreover, we found that the excitation beam actually contained components propagating at large off-axis angles (Figure S6, Supporting Information): when the central wavelength of the OPA was tuned to either longer or shorter side, SH emission corresponding to FW modes at relatively large excitation angles was also generated. Therefore, for a fixed FW, only a small fraction of the excitation beam with the right transverse wavevectors can excite the quasi-BIC modes at this FW and thus really contribute to SHG.

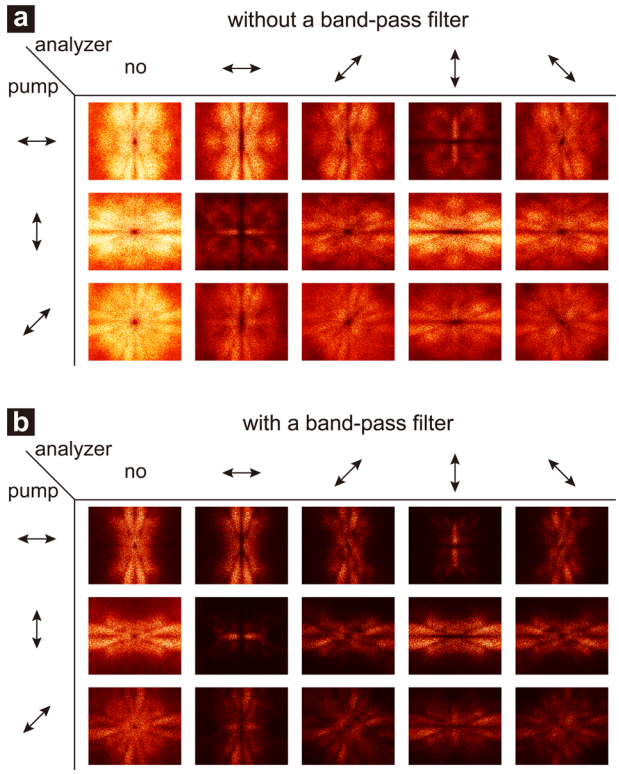

Figure 4. Far-field pattern of the (0, 0)-order SH emission. Images are captured a) without and b) with a 660 nm band-pass filter, respectively. Black arrows on the left indicate the polarization state of the pump, and those on top indicate the polarization direction of the linear polarizer in front of the camera. The image area is 8.45 mm × 7.07 mm.

From the enlarged views of the (0, 0) diffraction order (Figure 3f,g), we noticed that the SH emission along the surface normal was relatively weak. To further study the profile of the far-field emission, we captured the emission pattern of the (0, 0) diffraction order using a CMOS camera (BC207VIS, Thorlabs) at selected polarization directions by rotating a linear polarizer in front of the camera. There indeed existed a dark spot at the center of the image area for whatever input polarization (**Figure 4**a). The reason should be attributed to the nature of quasi-BIC modes at FW: when the input polarization was horizontal, those incident components propagating parallel to the vertical incident plane (with $k_x = 0$) could not couple to the nonlinear polarization due to symmetry mismatch; when the input polarization was vertical, those incident components propagating parallel to the horizontal incident plane (with $k_y = 0$) could not couple to the nonlinear polarization. The patterns in Figure 4a were a mixture with different wavelengths. We then used a band-pass filter (with a central wavelength of 660 nm and bandwidth of 10 nm) to isolate the strongest part (Figure 4b). We found that

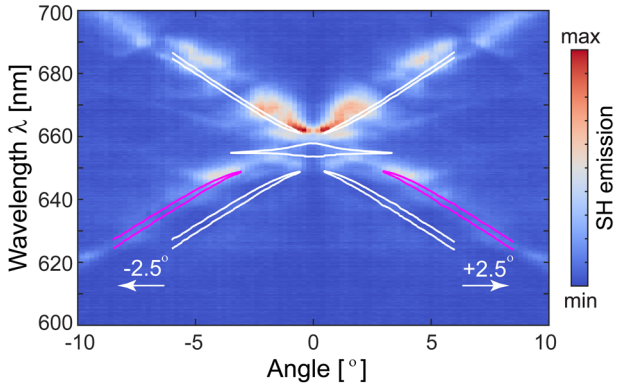

Figure 5. Relation between the FW excitation angles and the (0, 0)-order SH emission angles. The blue to red color map visualizes the dispersion of the SH emission in the *xz*-plane, obtained through adding up angle-resolved SH emission spectra under *x*-polarized pumping from OPA with the central wavelength tuned to 1280 and 1420 nm. The overlaid white lines are the trace of the white-light transmission spectra under TM polarization (with the wavelength axis divided by 2). The lines in magenta are the copy of the white ones ($\lambda < 650$ nm) but shifted horizontally by 2.5°.

there was emission with polarization orthogonal to the pump polarization, and the two orthogonal polarization states were spatially separated. We also analyzed the polarization states of the (±1, 0) and (0, ±1) diffraction orders at the angular positions exhibiting peak intensity: for horizontal (*x*) input polarization, the (±1, 0) diffraction orders were mostly *x*-polarized, while the (0, ±1) diffraction orders were mostly *y*-polarized.

Finally, we study the relation between the FW excitation angles and the (0, 0)-order SH emission angles. We discuss only the situation of Figure 3c where the SH emission spots were mostly *x*-polarized when the pump was also *x*-polarized (TM polarization). In other words, there was no rotation of polarization for this situation. As mentioned earlier, the excitation beam contained components propagating at large off-axis angles, and thus rotating the sample to change the excitation angle was not necessary. We added up the angle-resolved SH emission spectra under *x*-polarized pumping from OPA with the central wavelength tuned to 1280 and 1420 nm to visualize the dispersion of the SH emission (**Figure 5**). Further, the white-light transmission spectra under TM polarization (with the wavelength axis of Figure 3d divided by 2) were overlaid as the white lines on the above synthesized angle-resolved emission spectra. We can see that the relation between the angles of the SH emission and of the FW excitation is basically linear, and there is a constant offset of 2.5° for the lower bands. The emission angles of the (±1, 0) diffraction orders can then be deduced from those of the zeroth order using the grating equation, $\sin\phi_{\pm1} = \sin\phi_0 \pm \lambda_{SH}/a_0$.

3. Conclusion

To conclude, we demonstrated enhanced SHG from *z*-cut thin-film lithium niobate under linearly-polarized pumping. By comparing the linear dispersion at the fundamental wavelength with the nonlinear response, we confirmed that the resonant enhancement of SHG in the 2D periodic array was enabled by the quasi bound-states in the continuum (quasi-BIC modes) bearing strong E_z-component. The SH emission pattern of the (0, 0) diffraction order exhibited a dark spot at the center and contained emission with polarization orthogonal to the pump polarization. More degrees of freedom to control the SHG can be obtained through engineering the lattice symmetry. We expect that tunable resonant enhancement of SHG for practical applications is achievable by combining properly tailored optical resonances with the emerging material platform of thin-film LN which offers a wide transparency window and excellent nonlinearity.

4. Experimental Section

Characterization of SH Emission and White-Light Transmission

The sample was mounted on rotational stages to characterize the SH emission and the dispersion (Figure 3a). The broadband pulses used to excite SHG came from an optical parametric amplifier (OPA; TOPAS-Prime), which was pumped by a femtosecond pulsed laser (75 fs at 1 kHz repetition rate; Solstice ACE, Spectra-Physics). The OPA output contained spectral components from the visible to the near infrared regime, and therefore was first filtered using double-side polished silicon wafers, and then focused onto the sample with a fused silica lens ($f = 175$ mm). The sample was put at a distance away from the focus to prevent burns, and thus the excitation beam was actually divergent. At the sample position, the excitation spot was about 750 μm in diameter and the total OPA power was 4.19 mW. The SH signal was coupled into a spectrometer (USB4000, Ocean Optics) using an achromatic lens (with a diameter of 5.5 mm, a focal length of 11 mm, and at a distance of about 380 mm away from the sample) and a multimode fiber after blocking the transmitted OPA beam by a short-pass filter. For white-light transmission measurements, a supercontinuum source (SuperK COMPACT, NKT Photonics) was coupled into the same beam path using a flip mirror, and finally turned into an optical spectrum analyzer (AQ6370D, Yokogawa). To extract the quality factors, the Breit–Wigner–Fano model was used to fit the transmission spectra under collimated white-light illumination.

Supporting Information

Supporting Information is available from the Wiley Online Library or from the author.

Acknowledgements

X.Z., L.H., and X.G. contributed equally to this work. This work was partially supported by the National Key Research and Development Project of China (2019YFA0705000), National Natural Science Foundation of China (12074227, 12192254, 91750201, 11974218), Innovation Group of Jinan (2018GXRC010), Local Science and Technology Development Project of the Central Government (No. YDZX20203700001766), and Natural Science Foundation of Guangdong Province (2018A0303130056, 2020A1515010491). X.A. thanks Prof. L. Liu for helping with the ICP etching, and Profs. Y. Y. Ren, L. N. Zhao, Z. H. Han, and Z. Q. Hao for accessing the lasers and detectors.

Conflict of Interest

The authors declare no conflict of interest.

Data Availability Statement

The data that support the findings of this study are available from the corresponding author upon reasonable request.

Keywords

bound states in the continuum, lithium niobate, second-harmonic generation

Received: January 18, 2022
Revised: April 5, 2022
Published online:

[1] E. L. Wooten, K. M. Kissa, A. Yi-Yan, E. J. Murphy, D. A. Lafaw, P. F. Hallemeier, D. Maack, D. V. Attanasio, D. J. Fritz, G. J. McBrien, D. E. Bossi, *IEEE J. Sel. Top. Quantum Electron.* **2000**, *6*, 69.
[2] C. Wang, M. Zhang, X. Chen, M. Bertrand, A. Shams-Ansari, S. Chandrasekhar, P. Winzer, M. Loncar, *Nature* **2018**, *562*, 101.
[3] M. Li, J. Ling, Y. He, U. A. Javid, S. Xue, Q. Lin, *Nat. Commun.* **2020**, *11*, 4123.
[4] M. He, M. Xu, Y. Ren, J. Jian, Z. Ruan, Y. Xu, S. Gao, S. Sun, X. Wen, L. Zhou, L. Liu, C. Guo, H. Chen, S. Yu, L. Liu, X. Cai, *Nat. Photonics* **2019**, *13*, 359.
[5] T. Wang, P. Chen, C. Xu, Y. Zhang, D. Wei, X. Hu, G. Zhao, M. Xiao, S. Zhu, *Sci. China Technol. Sci.* **2020**, *63*, 1110.
[6] G. Poberaj, H. Hu, W. Sohler, P. Günter, *Laser Photonics Rev.* **2012**, *6*, 488.
[7] J. Lin, F. Bo, Y. Cheng, J. Xu, *Photonics Res.* **2020**, *8*, 1910.
[8] Y. Jia, L. Wang, F. Chen, *Appl. Phys. Rev.* **2021**, *8*, 011307.
[9] A. Boes, B. Corcoran, L. Chang, J. Bowers, A. Mitchell, *Laser Photonics Rev.* **2018**, *12*, 1700256.
[10] D. Zhu, L. Shao, M. Yu, R. Cheng, B. Desiatov, C. J. Xin, Y. Hu, J. Holzgrafe, S. Ghosh, A. Shams-Ansari, E. Puma, N. Sinclair, C. Reimer, M. Zhang, M. Lončar, *Adv. Opt. Photonics* **2021**, *13*, 242.
[11] C. Wang, Z. Li, M. H. Kim, X. Xiong, X. F. Ren, G. C. Guo, N. Yu, M. Loncar, *Nat. Commun.* **2017**, *8*, 2098.
[12] C. Wang, X. Xiong, N. Andrade, V. Venkataraman, X. F. Ren, G. C. Guo, M. Loncar, *Opt. Express* **2017**, *25*, 6963.
[13] C. Wang, C. Langrock, A. Marandi, M. Jankowski, M. Zhang, B. Desiatov, M. M. Fejer, M. Lončar, *Optica* **2018**, *5*, 1438.
[14] R. Luo, Y. He, H. Liang, M. Li, Q. Lin, *Laser Photonics Rev.* **2019**, *13*, 1800288.
[15] Y. Niu, C. Lin, X. Liu, Y. Chen, X. Hu, Y. Zhang, X. Cai, Y.-X. Gong, Z. Xie, S. Zhu, *Appl. Phys. Lett.* **2020**, *116*, 101104.
[16] J. Zhao, M. Rüsing, U. A. Javid, J. Ling, M. Li, Q. Lin, S. Mookherjea, *Opt. Express* **2020**, *28*, 19669.
[17] L. Wang, X. Zhang, F. Chen, *Laser Photonics Rev.* **2021**, *15*, 2100409.
[18] R. Luo, Y. He, H. Liang, M. Li, J. Ling, Q. Lin, *Phys. Rev. Appl.* **2019**, *11*, 034026.
[19] J. Lu, J. B. Surya, X. Liu, A. W. Bruch, Z. Gong, Y. Xu, H. X. Tang, *Optica* **2019**, *6*, 1455.
[20] C. Wang, M. J. Burek, Z. Lin, H. A. Atikian, V. Venkataraman, I. C. Huang, P. Stark, M. Loncar, *Opt. Express* **2014**, *22*, 30924.
[21] R. Wu, J. Zhang, N. Yao, W. Fang, L. Qiao, Z. Chai, J. Lin, Y. Cheng, *Opt. Lett.* **2018**, *43*, 4116.
[22] J. Lin, N. Yao, Z. Hao, J. Zhang, W. Mao, M. Wang, W. Chu, R. Wu, Z. Fang, L. Qiao, W. Fang, F. Bo, Y. Cheng, *Phys. Rev. Lett.* **2019**, *122*, 173903.
[23] X. Ye, S. Liu, Y. Chen, Y. Zheng, X. Chen, *Opt. Lett.* **2020**, *45*, 523.
[24] Z. Hao, L. Zhang, W. Mao, A. Gao, X. Gao, F. Gao, F. Bo, G. Zhang, J. Xu, *Photonics Res.* **2020**, *8*, 311.
[25] L. Zhang, Z. Hao, Q. Luo, A. Gao, R. Zhang, C. Yang, F. Gao, F. Bo, G. Zhang, J. Xu, *Opt. Lett.* **2020**, *45*, 3353.
[26] M. Li, H. Liang, R. Luo, Y. He, Q. Lin, *Laser Photonics Rev.* **2019**, *13*, 1800228.
[27] S. Diziain, R. Geiss, M. Zilk, F. Schrempel, E.-B. Kley, A. Tünnermann, T. Pertsch, *Appl. Phys. Lett.* **2013**, *103*, 051117.
[28] H. Jiang, H. Liang, R. Luo, X. Chen, Y. Chen, Q. Lin, *Appl. Phys. Lett.* **2018**, *113*, 021104.
[29] S. Yuan, Y. Wu, Z. Dang, C. Zeng, X. Qi, G. Guo, X. Ren, J. Xia, *Phys. Rev. Lett.* **2021**, *127*, 153901.
[30] G. Grinblat, Y. Li, M. P. Nielsen, R. F. Oulton, S. A. Maier, *Nano Lett.* **2016**, *16*, 4635.
[31] L. Xu, M. Rahmani, K. Zangeneh Kamali, A. Lamprianidis, L. Ghirardini, J. Sautter, R. Camacho-Morales, H. Chen, M. Parry, I. Staude, G. Zhang, D. Neshev, A. E. Miroshnichenko, *Light Sci. Appl.* **2018**, *7*, 44.
[32] M. Semmlinger, M. Zhang, M. L. Tseng, T. T. Huang, J. Yang, D. P. Tsai, P. Nordlander, N. J. Halas, *Nano Lett.* **2019**, *19*, 8972.
[33] Y. Yang, W. Wang, A. Boulesbaa, Kravchenko, II, D. P. Briggs, A. Puretzky, D. Geohegan, J. Valentine, *Nano Lett.* **2015**, *15*, 7388.
[34] K. Koshelev, Y. Tang, K. Li, D.-Y. Choi, G. Li, Y. Kivshar, *ACS Photonics* **2019**, *6*, 1639.
[35] N. Bernhardt, K. Koshelev, S. J. U. White, K. W. C. Meng, J. E. Froch, S. Kim, T. T. Tran, D. Y. Choi, Y. Kivshar, A. S. Solntsev, *Nano Lett.* **2020**, *20*, 5309.
[36] A. P. Anthur, H. Zhang, R. Paniagua-Dominguez, D. A. Kalashnikov, S. T. Ha, T. W. W. Mass, A. I. Kuznetsov, L. Krivitsky, *Nano Lett.* **2020**, *20*, 8745.
[37] F. J. F. Löchner, A. George, K. Koshelev, T. Bucher, E. Najafidehaghani, A. Fedotova, D.-Y. Choi, T. Pertsch, I. Staude, Y. Kivshar, A. Turchanin, F. Setzpfandt, *ACS Photonics* **2020**, *8*, 218.
[38] Z. Liu, Y. Xu, Y. Lin, J. Xiang, T. Feng, Q. Cao, J. Li, S. Lan, J. Liu, *Phys. Rev. Lett.* **2019**, *123*, 253901.
[39] Z. Liu, J. Wang, B. Chen, Y. Wei, W. Liu, J. Liu, *Nano Lett* **2021**, *21*, 7405.
[40] K. Koshelev, S. Kruk, E. Melik-Gaykazyan, J.-H. Choi, A. Bogdanov, H.-G. Park, Y. Kivshar, *Science* **2020**, *367*, 288.
[41] F. Monticone, D. Sounas, A. Krasnok, A. Alù, *ACS Photonics* **2019**, *6*, 3108.
[42] K. V. Baryshnikova, D. A. Smirnova, B. S. Luk'yanchuk, Y. S. Kivshar, *Adv. Opt. Mater.* **2019**, *7*, 1801350.
[43] A. E. Miroshnichenko, A. B. Evlyukhin, Y. F. Yu, R. M. Bakker, A. Chipouline, A. I. Kuznetsov, B. Luk'yanchuk, B. N. Chichkov, Y. S. Kivshar, *Nat. Commun.* **2015**, *6*, 8069.
[44] C. W. Hsu, B. Zhen, A. D. Stone, J. D. Joannopoulos, M. Soljačić, *Nat. Rev. Mater.* **2016**, *1*, 16048.
[45] K. Koshelev, S. Lepeshov, M. Liu, A. Bogdanov, Y. Kivshar, *Phys. Rev. Lett.* **2018**, *121*, 193903.
[46] J. Ma, F. Xie, W. Chen, J. Chen, W. Wu, W. Liu, Y. Chen, W. Cai, M. Ren, J. Xu, *Laser Photonics Rev.* **2021**, *15*, 2000521.
[47] A. Fedotova, M. Younesi, J. Sautter, A. Vaskin, F. J. F. Lochner, M. Steinert, R. Geiss, T. Pertsch, I. Staude, F. Setzpfandt, *Nano Lett.* **2020**, *20*, 8608.
[48] L. Carletti, A. Zilli, F. Moia, A. Toma, M. Finazzi, C. De Angelis, D. N. Neshev, M. Celebrano, *ACS Photonics* **2021**, *8*, 731.
[49] B. Gao, M. Ren, W. Wu, W. Cai, J. Xu, *Sci. China Phys.* **2021**, *64*, 240362.
[50] L. Kang, H. Bao, D. H. Werner, *Opt. Lett.* **2021**, *46*, 633.
[51] Q. Yang, Y. Liu, X. Gan, C. Fang, G. Han, Y. Hao, *IEEE Photon. J.* **2020**, *12*, 1.
[52] Z. Huang, M. Wang, Y. Li, J. Shang, K. Li, W. Qiu, J. Dong, H. Guan, Z. Chen, H. Lu, *Nanotechnology* **2021**, *32*, 325207.
[53] K.-H. Kim, W.-S. Rim, *ACS Photonics* **2018**, *5*, 4769.
[54] X. Ao, D. Wang, T. W. Odom, *ACS Photonics* **2019**, *6*, 2612.
[55] J. Jin, X. Yin, L. Ni, M. Soljacic, B. Zhen, C. Peng, *Nature* **2019**, *574*, 501.

